Landmark Navigation and Target Characterization in a
Simulated Itokawa Encounter

Robert W. Gaskell
MS 301/150 Jet Propulsion Laboratory
California Institute of Technology
4800 Oak Grove Drive, Pasadena. CA 91109
818 354-2116
rwg@jpl.nasa.gov

Abstract

A simulated asteroid Itokawa was constructed from Ostro's latest radar model adding craters, rocks and fractal surfacing. Images were constructed from this model with known spacecraft positions and orientations, and asteroid pole and shape as "ground truth", using available values for the Hayabusa camera parameters, and following the proposed encounter scenario. The nominal values of these quantities were given realistic errors. The images were analyzed with landmark navigation and target characterization software to determine how well ground truth could be reproduced. Calculated spacecraft locations during approach to the surface agreed with the true values to less than a meter.

1. Introduction

In September, the Japanese Hayabusa spacecraft will arrive at the asteroid 25143 Itokawa. Due to Itokawa's small size (600 meters) and low gravity, the spacecraft will not orbit, but will hover near each of three stations; one at a range of ~20 km on a line between the asteroid and Earth, one on the same line at ~7 km, and one ~45 ^{o} around the

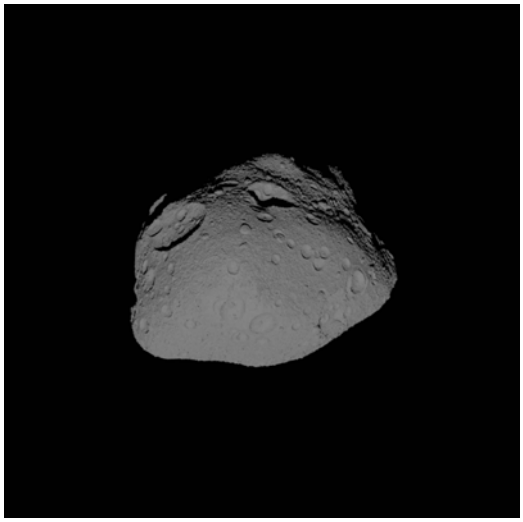

Figure 1. Simulated Itokawa image

body, again at ~7 km. After observing Itokawa for two months, the spacecraft will make

a test approach in November and then will touch down twice, collecting samples for return to Earth.

The clever simplicity of this encounter made an ideal simulation for testing landmark navigation and target characterization software (Gaskell, 2001, 2002, 2003). 84 narrow-angle images were "taken" at each of the two full-phase stations, and 28 at the 45° phase station. At the first two, the spacecraft was allowed to drift 3 and 2 km respectively northward and southward. Thirteen wide-angle images were taken during the test approach. Figure 1 shows a typical narrow-angle frame. These images were made from a 1,572,866-vector model based on the most recent radar shape (Ostro, et al. 2004) with added craters, rocks and fractal surfacing. The pole at RA=160°, DEC=-89°, and the input spacecraft positions and orientations, provided the "truth".

The nominal states were then given realistic errors. The spacecraft location had rms errors 0.1% of range in each component, while the errors in the camera pointing were 0.25 mrad per axis. The nominal pole was taken to be RA=163°, DEC=-86°, different from the "true" pole from which the images were constructed. Finally, the nominal shape was taken to be Ostro's 2001 radar model, which differs significantly from his 2004 result. The rotation rate of 712.14445 deg/day remained fixed.

Starting with the images created from "truth" and using the messed up nominals, the goal was to see how closely the truth could be recovered. The fundamental data product of this study was the digital topographic landmark map (L-map), constructed from imaging data by using stereophotoclinometry (SPC) to find surface slopes, which were then integrated to determine topography. Figure 2 shows such an L-map in the context of an Eros shape model, created as part of an ongoing analysis of the NEAR imaging data (Gaskell, 2004). L-map specifications include a local coordinate

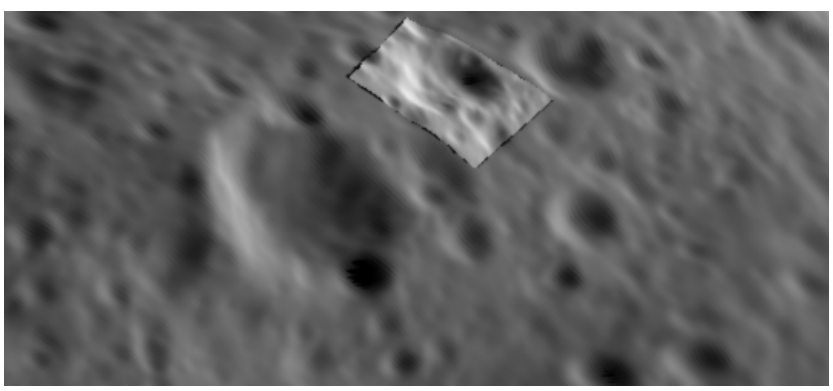

Figure 2. Landmark map in Eros shape model

system, the surface heights relative to that coordinate system, with the central pixel having zero height, the relative albedo at each map pixel, and the vector from the center of the body to the central pixel of the L-map. Because of their three-dimensional structure, landmark maps can be aligned with images, limbs and other maps to find landmark location and spacecraft position and orientation. They can also be combined to

produce a detailed shape model, or high-resolution topographic map for any portion of the surface. The errors in this approach are at least an order of magnitude smaller than either traditional stereography or laser altimetry, and the resolution is considerably higher.

This paper is divided into two parts. The first part collects the principal algorithms used in the study, while the second part gives a blow-by-blow description of the study itself. Section 2 discusses the projection of the imaging data into the coordinate frame of an L-map, the illumination of the L-map for correlation with the image projection, and the correlation of L-maps with limb data and with other L-maps. Section 3 deals with the geometry estimation that uses the correlation data to solve for L-map vectors and spacecraft position and orientation. Section 4 discusses the construction of an L-map, using SPC to determine the slope and relative albedo distribution, and the subsequent integration of the slopes to produce the final digital elevation map. Section 5 deals with the synthesis of shape models and high-resolution topographic maps from the set of L-maps. Section 6 discusses the creation of the simulated Itokawa data while section 7 describes the four-week real-time solution for the L-maps and spacecraft geometry. In section 8, the results are applied to navigation during proximity operations.

As in any useful simulation, this study exposed many errors and suggested many changes. Some of what has been learned is discussed in section 9. This will make things run more smoothly when it is done for real starting next month.

2. L-map to image connection

At the heart of the analysis is the connection between the location of a pixel on an L-map and its predicted location in an image. This connection depends upon the location, orientation and height variation of the L-map, the location and orientation of the camera (spacecraft), and the rotational dynamics of the body. A change in any of these quantities results in a characteristic change in the image-space projections, leading to their estimation in terms of the imaging data.

An L-map is specified by a vector **V** from the center of a body fixed coordinate system to the origin of the L-map coordinate system, by the axes of that coordinate system $\mathbf{u}_i$ (i=1,3), and by heights and albedos at positions (x,y) relative to that system. The L-map coordinates of a body-fixed point **P** on the surface are $x=\mathbf{u}_1\bullet(\mathbf{P}-\mathbf{V})$ and $y=\mathbf{u}_2\bullet(\mathbf{P}-\mathbf{V})$ with the height $h(x,y)=\mathbf{u}_3\bullet(\mathbf{P}-\mathbf{V})$ and an albedo a(x,y). The camera's position vector **W** and its coordinate system $\mathbf{c}_i$ (i=1,3), unit vectors in the sample, line and boresight directions, respectively, are also specified in body-fixed coordinates.

For a simple narrow angle camera with focal length f, the focal plane image location X_i (i=1,2) of the L-map center **V** is given by

1) $X_i = f(\mathbf{V}-\mathbf{W})\bullet\mathbf{c}_i/(\mathbf{V}-\mathbf{W})\bullet\mathbf{c}_3$

If $M_{ij}=\mathbf{c}_i\bullet\mathbf{u}_j$, a point (x,y,h) on the L-map has the focal plane projection

2) $X_i = f((\mathbf{V}-\mathbf{W})\bullet\mathbf{c}_i+M_{i1}x+M_{i2}y+M_{i3}h)/((\mathbf{V}-\mathbf{W})\bullet\mathbf{c}_3+M_{31}x+M_{32}y+M_{33}h)$

An equally important connection is between the slopes and albedos within an L-map, the local illumination and camera directions, and the predicted image-space brightness. A change in slope or albedo at any L-map pixel will result in a characteristic change in the predicted brightness at the corresponding location in an image. At the point (x,y) of the L-map, the brightness at the corresponding focal plane location in the kth image can be parameterized as

3) $I_k(x,y,\mathbf{t}) = \Lambda_k(1+t_3(x,y))F(\cos i,\cos e) + \Phi_k$

F is an appropriate reflectance function (Hapke,1981; Squyres and Veverka, 1982). The factor $(1+t_3)$ is the relative albedo at map coordinates (x,y), normalized so that $\langle t_3\rangle=0$ over the map, and *i* and *e* are the local angles of incidence and emission, relative to the surface normal at (x,y). During its extraction, the imaging data is usually scaled (maximally stretched), so the multiplier Λ_k is included. Moreover, due to background or haze in some images, or perhaps because super-resolution sampling has left a "washed out" look, a positive background term Φ_k can be added.

In terms of the (negative) slopes t_1=-dh/dx and t_2=-dh/dy, the local arguments of the function F are

4a) $\cos i = (s_1t_1+s_2t_2+s_3)/\sqrt{(1+t_1^2+t_2^2)}$

4b) $\cos e = (e_1t_1+e_2t_2+e_3)/\sqrt{(1+t_1^2+t_2^2)}$

where $s_j= \mathbf{s}\bullet\mathbf{u}_j$ and $e_j = \mathbf{e}\bullet\mathbf{u}_j$ are the L-map components of the sun and spacecraft unit vectors respectively. The reflectance function

5) $F(\cos i,\cos e) = \cos i + 2\cos i/(\cos i+\cos e)$

is used, since it does a good job rendering high resolution shape models. No phase dependence has been included since it is nearly constant over each L-map, even for wide-angle images, and any phase functions can be absorbed into Λ_k .

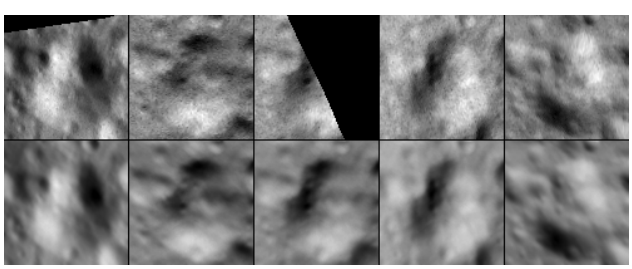

Figure 3. Imaging data and re-illuminated L-map

The top row of Fig. 3 displays data extracted from five NEAR images, projected onto the coordinates of the L-map displayed in Fig. 2 according to equation 2). The

bottom row shows the corresponding L-map illuminated according to equation 3), with the Λ_k adjusted to match the average brightness in the overlapping regions.

In addition to its appearance on the image of a body, the three-dimensional structure of an L-map allows it to be identified on the limb. Fig. 4 shows the same L-map as it appears on the limb of a NEAR image reconstructed from the Eros shape model. The focal plane location of the map center, which is not necessarily on the limb, is still determined by equation 2). The predicted limb points are those parts of the L-map surface to which the line of sight is tangent, and which are not either hiding or hidden by any other part of the body.

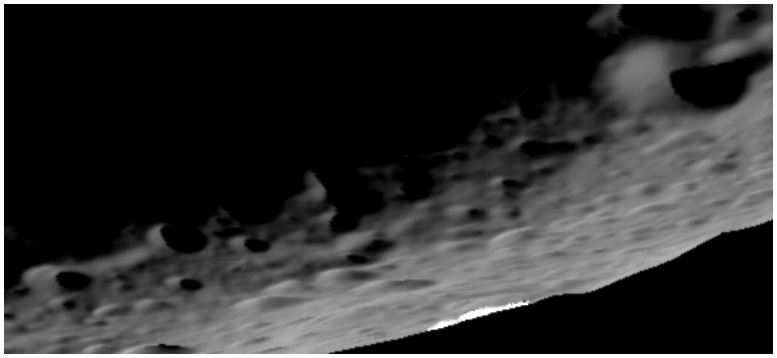

Figure 4. Appearance of the L-map on a limb.

A final constraint on the L-map lies not with its correlation with imaging data, but with other L-maps. The common topography of the overlapping maps can be aligned in three-dimensions to solve for the central vector **V** of one L-map relative to the other.

3. Geometry estimation

The geometry problem consists of determining the body fixed L-map vectors **V**, the body's pole, and the spacecraft location **W** and orientation **c**. The L-map topography problem is treated as a separate estimation. The geometry solution is found by minimizing the quantity

6) $$H = \Sigma K(Y_i - X_i)^2 + H_E$$

with respect to variations in **V**, **W**, **c**, or the pole. Y_i (i=1,2) are the measured focal plane locations of the L-map centers and where the predicted locations X_i (i=1,2) come from equation 1). The sum is over all L-maps and all images, with each term weighted by a different "spring constant" K, the inverse square measurement uncertainty. The H_E represent external *a priori* terms which constrain the estimation according to external measurements. The solution proceeds iteratively, solving in turn for all the L-map vectors **V**, and then for the spacecraft positions and orientations **W** and **c**. Formal uncertainties from each solution help determine the weights K of the next.

The solution for an L-map vector $\mathbf{V} + \delta\mathbf{V}$ is found by minimizing

7) $$H = \Sigma K(Y_i - X_i - \delta\mathbf{V}\bullet\nabla_V X_i)^2 + \Sigma K_m (\mathbf{V}_m + \Delta_m - \mathbf{V} - \delta\mathbf{V})^2$$

where X_i is evaluated at the nominal vector $\mathbf{V}$, and $\nabla_V X_i$ are the partials of X_i with respect to the components of $\mathbf{V}$. The first sum is over all images containing the landmark, while the second, coming from H_E, is over all overlapping L-maps. Δ_m is the difference between the two central L-map vectors from the correlation discussed at the end of Section 2. The minimum of H in equation 7) occurs when

8) $$\Sigma K\nabla_V X_i (Y_i - X_i - \nabla_V X_i \bullet\delta\mathbf{V}) + \Sigma K_m (\mathbf{V}_m + \Delta_m - \mathbf{V} - \delta\mathbf{V}) = 0$$

which can be written as

9) $$\mathbf{M}\bullet\delta\mathbf{V} = \mathbf{r}$$

with $\mathbf{M} = \Sigma K\nabla_V X_i \otimes \nabla_V X_i + \Sigma K_m \mathbf{I}$ and $\mathbf{r} = \Sigma K\nabla_V X_i(Y_i - X_i) + \Sigma K_m(\mathbf{V}_m + \Delta_m - \mathbf{V})$. The 3x3 matrix $\mathbf{M}$ is inverted to solve equation 9) for the corrections $\delta\mathbf{V} = \mathbf{M}^{-1}\bullet\mathbf{r}$. The diagonal elements of $\mathbf{M}^{-1}$ are the squares of the formal uncertainties in $\mathbf{V}$.

The solutions for spacecraft position $\mathbf{W} + \delta\mathbf{W}$ and orientation $\mathbf{c}_i + \varepsilon_{ijk}\mathbf{c}_j\delta\alpha_k$ are found by minimizing

10) $$H = \Sigma K(Y_i - X_i - \delta\mathbf{W}\bullet\nabla_W X_i - \delta\boldsymbol{\alpha}\bullet\nabla_\alpha X_i)^2 + K_n(\mathbf{W}_n - \mathbf{W} - \delta\mathbf{W})^2$$

$$+ K_n(\varepsilon_{ijk}\, \mathbf{c}_{ni}\bullet\mathbf{c}_j - \delta\alpha_k)^2 + \Sigma K_p(\mathbf{W}_p + \Delta_p - \mathbf{W} - \delta\mathbf{W})^2$$

The sum in the first term is over all landmarks occurring in the image, with the K determined from the formal uncertainties of the previous estimation. The second two terms reflect nominal positions, orientations and, through the K_n, the corresponding uncertainties. These come, for example, from external radiometric, optical navigation and star-tracker measurements. The final term is a sum over those images correlated with the image in question, those that are close enough in time so that the position difference Δ_p can be predicted by the trajectory dynamics. This term ties images together in the same way that the last term in equation 7) ties L-maps together. The minimization of H in equation 10) results in a set of six equations for the six corrections $\delta\mathbf{W}$ and $\delta\boldsymbol{\alpha}$.

A change in the rotation of the body alters the components of the vectors in the body-fixed frame in a time-dependent fashion. It does not affect the scalars $\mathbf{W}\bullet\mathbf{c}$ in equation 1) since both vectors are associated with a single image and are transformed in the same way. The products $\mathbf{V}\bullet\mathbf{c}$ will change, however, both because the components of $\mathbf{V}$ and the $\mathbf{c}$ change, and because the new geometry yields a new solution for the L-map vectors. The corrections to the rotational parameters $\mathbf{g}$ and the L-map vectors $\mathbf{V}$ are determined by minimizing

11) $H = \Sigma K(Y_i - X_i - \delta\mathbf{g}\bullet\nabla_g X_i - \delta\mathbf{V}\bullet\nabla_V X_i)^2$

summed over all images and all landmarks. The resulting equations are

12) $\mathbf{A}\bullet\delta\mathbf{g} + \Sigma\, \mathbf{C}_k^{\mathbf{T}}\bullet\delta\mathbf{V}_k = \mathbf{r}_0$ and $\mathbf{C}_k\bullet\delta\mathbf{g} + \mathbf{B}_k\bullet\delta\mathbf{V}_k = \mathbf{r}_k$

where k labels the L-maps and

13)
$\mathbf{A} = \Sigma K\nabla_g X_i \otimes\nabla_g X_i$ (sum over all images and L-maps)
$\mathbf{B}_k = \Sigma K\nabla_{Vk} X_i \otimes\nabla_{Vk} X_i$ (sum over all images with L-map k)
$\mathbf{C}_k = \Sigma K\nabla_{Vk} X_i \otimes\nabla_g X_i$ (sum over all images with L-map k)
$\mathbf{r}_0 = \Sigma K(Y_i - X_i)\nabla_g X_i$ (sum over all images and L-maps)
$\mathbf{r}_k = \Sigma K(Y_i - X_i)\nabla_{Vk} X_i$ (sum over all images with L-map k)

In practice, the $\delta\mathbf{V}$ are eliminated from equations 12) to give

14) $(\mathbf{A} - \Sigma\, \mathbf{C}_k^{\mathbf{T}}\mathbf{B}_k^{-1}\mathbf{C}_k)\bullet\delta\mathbf{g} = \mathbf{r}_0 - \Sigma\, \mathbf{C}_k^{\mathbf{T}}\mathbf{B}_k^{-1}\mathbf{r}_k$

which is solved for the rotational correction $\delta\mathbf{g}$. The spacecraft positions **W** and orientations **c** are then expressed in the new body-fixed frame and equation 9) is used to find the new L-map vectors **V**.

4. Topography estimation

Each L-map is typically about a hundred pixels square. At each of these pixels (x,y), the values of t_i are solved for, fitting the extracted brightness data $E_k(x,y)$ to equation 3) by minimizing the weighted sum squared residual

15) $H = \Sigma K\,(E_k(x,y) - I_k(x,y,\mathbf{t}) - \delta t\bullet\nabla_t I_k(x,y,t))^2$

where the sum is over the images. Λ and Φ are determined from a global fit over the L-map at the nominal values of **t**.

The minimization of H is accomplished by setting its partials with respect to $\delta\mathbf{t}$ equal to zero. This yields a set of three coupled linear equations of the form $\mathbf{M}\delta\mathbf{t} = \mathbf{w}$, where the information matrix **M** is quadratic in the partials of I, and **w** is made up of products of the partials and the residuals. The inverse of the information matrix, $\mathbf{M}^{-1}$, is the covariance matrix. Its diagonal elements measure the formal uncertainties σ^2 in the corresponding variables. To **M** is added a diagonal *a priori* information matrix **D** to keep the solution from diverging. In particular, if the albedo component D_{33} is large, albedo variations will be tightly constrained. This is often done initially, to allow time for the topography solution to settle down.

Notice that the slopes determined in this way do not implicitly satisfy the "curl-free" condition $\partial_1 t_2 - \partial_2 t_1 = 0$, which follows from $\partial_1\partial_2 h - \partial_2\partial_1 h = 0$. However, the nominal values of t_1 and t_2 used in the estimation are found from the height solutions described

below and are manifestly curl-free, so as the iteration proceeds, the condition is eventually satisfied.

The height at each location (x,y) is determined from the neighboring heights, and a possible constraining height h_c from the shape model, differential stereography, limb or overlapping map data, according to:

$$16)\quad h(x,y) = [h(x+s,y)+s(t_1(x,y)+t_1(x+s,y))/2+h(x-s,y)-s(t_1(x,y)+t_1(x-s,y))/2 +h(x,y+s)+s(t_2(x,y)+t_2(x,y+s))/2+h(x,y-s)-s(t_2(x,y)+t_2(x,y-s))/2 +w_c h_c(x,y)+]/(w_c+4),$$

where s is the map pixel spacing and w_c is a small constraining weight. This equation is applied repeatedly to map points chosen at random until a converged solution is reached. If any height does not exist, its term is not included in the average. Fig. 5a shows the landmark map displayed in Fig. 2. Fig. 5b shows the locations of the constraining heights. The connected points come from limb projections in 26 images, while the isolated points come from sparsely sampled heights in overlapping maps, such as the one shown in Fig. 5c.

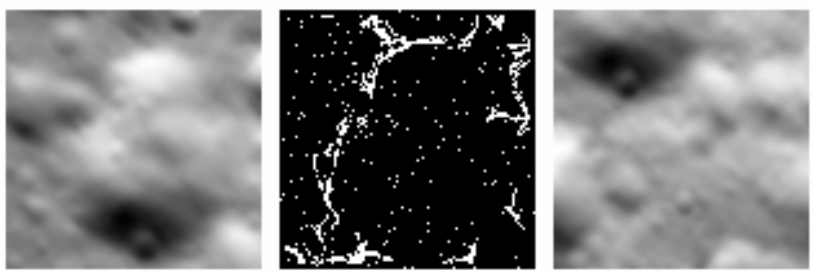

Figure 5. a) Landmark map. b) Constraining points. c) Overlapping map

5. Shape and topography models.

As the number of landmarks increases, a nearly rigid network of fixed surface points constrains the solutions for **c**, **W**, and **V**. Moreover, since each landmark map contains about 10,000 pixels, each at a well-defined location relative to the central vector **V**, the surface is described by a vast amount of data. The current Eros model, for example, has more than 4900 landmarks, giving over 49 million surface points.

The first step in the construction of the shape is the choice of a set of direction vectors for an initial rough model. In order to avoid the pole singularities of a spherical coordinate system, grid points on the faces of a cube are chosen as in Fig. 6. These direction vectors maintain their implicit connectivity as the initial defining solid is deformed, so that a separate listing of vertex connections is not necessary.

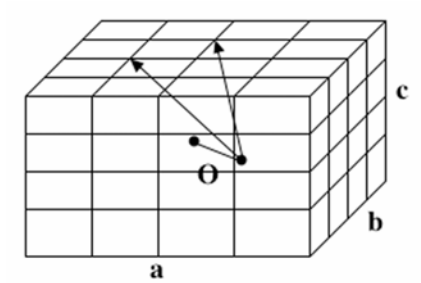

Figure 6. Initial direction vectors.

65x65 grids are typically used, providing about 25,000 direction vectors. The surface vectors are then projected onto this set. Once this initial model is found, a new set of direction vectors is constructed by stretching the cube into a rectangular solid with edges a, b, and c, and shifting the center by an offset vector **O**. These parameters are chosen in order to equalize the surface areas of the shape model corresponding to each of the six faces. The resulting distribution is shown in Fig. 7a. The intersections of the grid lines within each face are then deformed in order to most nearly equalize the surface area projections of the cells on that face. The revised distribution is illustrated in Fig. 7b.

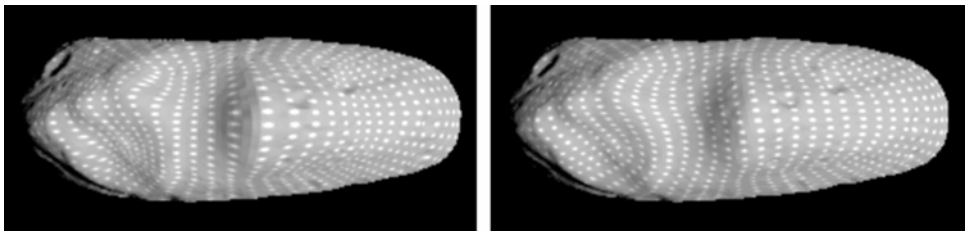

Figure 7. Distributions after a) face area equalization, b) cell area equalization.

By construction, this model is single-valued in radius as a function of direction. This is not in general the case for real surfaces, and in particular for the surface of Eros. This preliminary model is used as a reference surface for the construction of the final model.

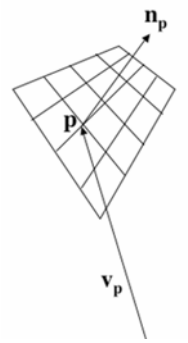

Figure 8. Vector and normal at a point in a subdivided cell.

The final model is constructed by subdividing each cell, and by constructing a vector and normal for each new vertex point by bilinear interpolation as in Fig. 8. Typically, each cell is divided into an 8x8 grid, providing a final set of about 1.57 million vectors. If $\mathbf{n_p}$ pierces a map, the distance along $\mathbf{n_p}$ from $\mathbf{p}$ to the intersection is called its height h. The weighted average of the heights of all such map intersections $h_p = \langle h \rangle$ is the height associated with the reference surface point $\mathbf{p}$. The surface vector $\mathbf{V_p}$ associated with $\mathbf{p}$ could be determined directly from h_p by

17) $\mathbf{V_p} = \mathbf{v_p} + \mathbf{n_p} h_p$.

It seems to be cleaner, however, to find the map normals $\mathbf{n}$ at each intersection point and then to associate their weighted average $\boldsymbol{\eta_p} = \langle \mathbf{n} \rangle$ with the point $\mathbf{p}$. Notice that the local normal $\boldsymbol{\eta_p}$ is not the same as the normal to the reference surface $\mathbf{n_p}$. If $\mathbf{p}$ and $\mathbf{q}$ are two neighboring surface points then $(\boldsymbol{\eta_p}+\boldsymbol{\eta_q})\bullet(\mathbf{V_p}-\mathbf{V_q})=0$ so the height at $\mathbf{p}$ can be found in terms of the nearest neighbor heights h_q and a possible constraining height h_{pc} at p by

18) $h_p = (w_c h_{pc} + \Sigma(\boldsymbol{\eta_p}+\boldsymbol{\eta_q})\bullet(\mathbf{v_q}-\mathbf{v_p}+\mathbf{n_q} h_q)/(\boldsymbol{\eta_p}+\boldsymbol{\eta_q})\bullet\mathbf{n_p})/(w_c+4)$.

The sum in Equation 18) is over nearest neighbors, h_{pc} is fixed at the weighted average height $\langle h \rangle$ described above and w_c is a small constraining weight. As in Equation 16), this is applied repeatedly to the reference surface points chosen at random until a converged solution is reached. If any height does not exist, its term is not included in the average. After the integration is complete, the heights are substituted into Equation 17) to find the surface vectors.

The corner vectors defining a cell on one of the faces of the final shape model, $\mathbf{v}(i,j)$, $\mathbf{v}(i+1,j)$, $\mathbf{v}(i,j+1)$ and $\mathbf{v}(i+1,j+1)$, define an approximate prism. The area vector of the cell is

19) $d\mathbf{A} = (\mathbf{v}(i+1,j+1)-\mathbf{v}(i,j))\mathbf{x}(\mathbf{v}(i+1,j)-\mathbf{v}(i,j+1))/2$.

If $\mathbf{v}$ is the average of the four corner vectors, and R is its magnitude, then the differential solid angle is

20) $d\Omega = \mathbf{v} \bullet d\mathbf{A}/R^3$.

This allows for very rapid calculations of physical properties of the model such as surface area, volume, moment of inertia tensor, and gravity harmonics. Notice that $d\Omega$ can be negative for some cells, indicating that a radius vector pierces the surface multiple times.

A similar procedure of averaging slopes and then integrating, this time referred to a local cartesian coordinate system, is used to combine L-maps into large, high resolution topographic maps of regions of interest. Fig. 9, for example, shows two orthogonal illuminations of a 1025x1025 pixel map of the center of Shoemaker Regio on Eros.

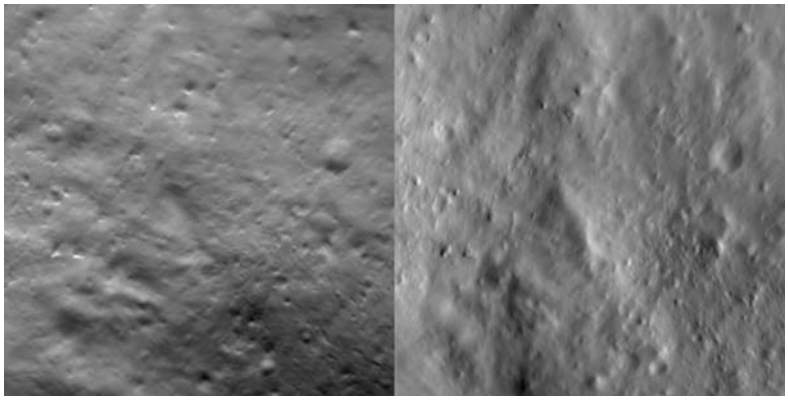

Figure9. High-resolution topography in Shoemaker Regio of Eros.

6. Initialization of the simulation

The simulation began with the construction of a model Itokawa, starting with Steve Ostro's latest radar model (Ostro, 2004), and adding craters, rocks and fractal surfacing (Gaskell, 2005). Ostro's Itokawa pole and rotation rate RA=160°, DEC=-89°, ω=712.14445 deg/day were used to define the body-fixed coordinate system. Imaging times and spacecraft positions and orientations were chosen, and images were created using the Itokawa model and realistic camera parameters.

An older Ostro model for Itokawa provided the nominal shape for the study. It was tiled with 215 overlapping L-maps, 99x99 pixel maps at 1.0 meter resolution. Two

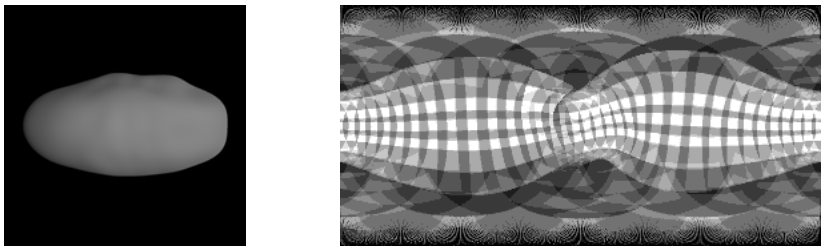

Figure 10. Nominal Itokawa shape and initial L-map tiling

files are associated with each L-map. First, the landmark file (.LMK) contains the nominal landmark vector, unit vectors defining its orientation, spaces for its location in images, both on the body and as limbs, and spaces to define its overlaps with other maps. Landmark files provide inputs to the geometry estimation of equation 6) in section 3, which then updates the landmark vector. Second, the map file (.MAP) also contains the central vector and orientation, but its remaining contents are the digital topography and albedo maps determined from the topography estimation of section 4, and for which this initial file provides the nominal topography. Creating these files beforehand saves valuable processing time during the encounter and, while they do not participate in the geometry estimation until images are added, they do provide one way in which to prevent

the origin of the coordinate system from drifting too far from the center of the body during initial processing.

The rotation rate for the nominal model remained the same, but the pole was taken to be RA=163°, DEC=-86°. The same observation times were used, but the nominal spacecraft positions and orientations were randomly altered, the former by 0.1% of range in each component and the latter by 0.25 mrad about each axis. For each image, a picture summary (.SUM) and nominals (.NOM) file were created. The first contains information about the camera parameters, the spacecraft's nominal position and orientation, and spaces for landmark locations in the image both on the body and on the limb. Together, the ensemble of landmark and summary files contain the information that would ordinarily be found in an OPNAV picture sequence file. The nominals file contains the nominal position and pointing information, and relative spacecraft locations coming, from trajectory dynamics, along with uncertainties on all of these quantities. The summary and nominals files are the inputs to the geometry estimation of section 3, which updates the spacecraft location and orientation in the summary file.

7. Narrow-angle processing

The analysis was started with the first set of 28 images from the 20 km station. Initial registration of the images was accomplished by manually aligning the projected imaging data in a display such as Fig. 3 or Fig. 13a below for a number of landmarks, and then carrying out the geometry solution of Section 3. The 99x99 pixel map size was chosen since, with a one pixel blank space between display blocks, feature locations in each block should be the same, modulo 100. If the pointing for an image is particularly bad, the initial registration can be carried out by aligning a projection of the image with the current global model, as in Fig. 11.

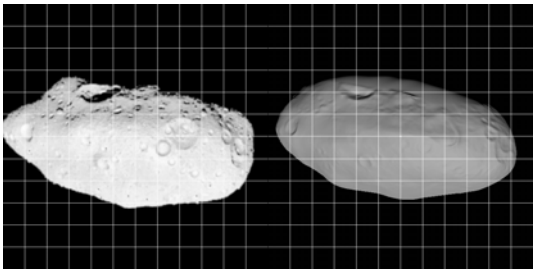

Figure 11. Registration by comparing image with current global model.

Processing of the first images took three days, and topography was found for 178 of the 215 original maps, shown below in Fig. 12. The poles were not covered, because pole-ward excursions of the spacecraft were not included in the image set. The alignment wasmore difficult than expected, for reasons which would not become clear for several weeks.

Figure 12. Image of 178 L-maps.

During the next week, 140 additional images were added from the two high phase stations. The existing landmark maps greatly speeded up the image registration. There are two ways to do this registration. First, a prominent landmark can be found in the set of all new images and correlated with extracted imaging data as in Fig. 13a). Second, all landmarks in a single image can be correlated with extracted imaging data, leading to an immediate solution for pointing and spacecraft location as in Fig. 13b).

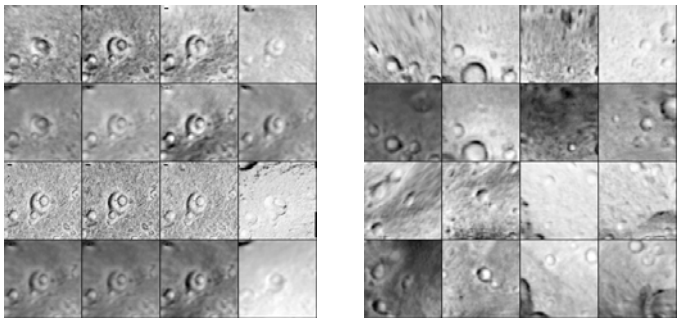

Figure 13. Alignment of a) a single landmark and b) a single image

The first and third lines of these displays are data extracted from the image(s). The second and fourth are illuminated L-map(s).

The first method was chosen. Many of the landmark maps were still distorted, so each landmark had to be reprocessed to include all relevant images. The maps now

Figure 14. a) Image of L-maps, b) global model, c) model after pole re-orientation

covered most of the body, because poleward excursions of the spacecraft allowed those regions to be mapped. A new global model was constructed from the maps. The first pole solution was found at RA = 161.6 ^{o}, DEC = -88.06 ^{o}, considerably closer to the true value than was the nominal. With the new pole, it was necessary to re-fit the maps in a nine-hour batch run. The resulting global model looked slightly different, in part because the solution was converging, but also because the body was oriented differently due to the updated pole.

At this point, about two weeks into the simulation, a major problem was found that accounted for the landmark distortions mentioned above. The differences between the calculated and exact spacecraft locations were over a hundred meters. At first, it was thought that the aliasing between pointing and spacecraft location was dominating the *a priori*. A few days later, it was found that an embarrassing error in accounting for light time corrections had left the nominal locations off by an average of 170 meters. The tight 20 m *a priori* had prevented the solution from converging to the correct values.

Once the nominals were corrected, things settled down. During the third – fifth iterations, taking another three days, the pole went from 162.20 ^{o}, -88.78 ^{o}, an error of 0.23 degrees, to 161.46 ^{o} ± 1.12, -88.97 ^{o} ± 0.04, an error of 0.38 degrees, to 160.27 ^{o} ± 1.34, -89.00 ^{o} ± 0.04, an error of 0.005 degrees.

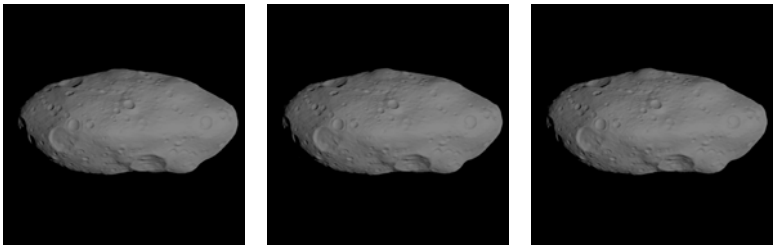

Figure 15. Successive global models after iterations 3, 4 and 5.

During the next four days, several hundred 0.5 meter resolution maps were added, bring the total to 494, and the 28 terminator station images were included. The global model became more detailed and the pole remained virtually fixed. No high-resolution

Figure 16. Converged global model.

maps were added near the poles due to unfavorable viewing geometry. The rms residuals in pointing were dominated by the tight *a priori*, as were the range residuals. The cross line-of-sight errors decreased to 3.5 m at the 20 km station and to 1.3 m at the 7 km station.

This point marked four weeks to the day since the simulation began. Despite major blunders and on-the-fly software rewrites, a database of nearly 500 landmarks has been created for use in proximity optical navigation. Moreover, the global model can be used to estimate the gravitational field near the surface in preparation for touchdown, and large, high-resolution maps synthesized from the L-maps can be used to characterize possible landing sites.

8. Proximity navigation

Seven wide-angle frames were constructed, representing views that might be taken during approach. They had ranges from 1000 m to 400 m, in 100 meter steps, and phases of 45 degrees to 15 degrees in 5 degree steps. The nominal locations had rms errors of 1.0% of range per component, but the camera pointing maintained the same 0.25 mrad random errors. The seven images were registered against the landmark set in less than ten minutes, solving for pointing and s/c location. Below is a typical alignment display from the 600 meter image. As in Fig. 13, odd lines are extracted imaging data and even lines are illuminated landmark maps. Although the L-maps do not have the same resolution as the actual images, the correlation algorithm had no trouble aligning them.

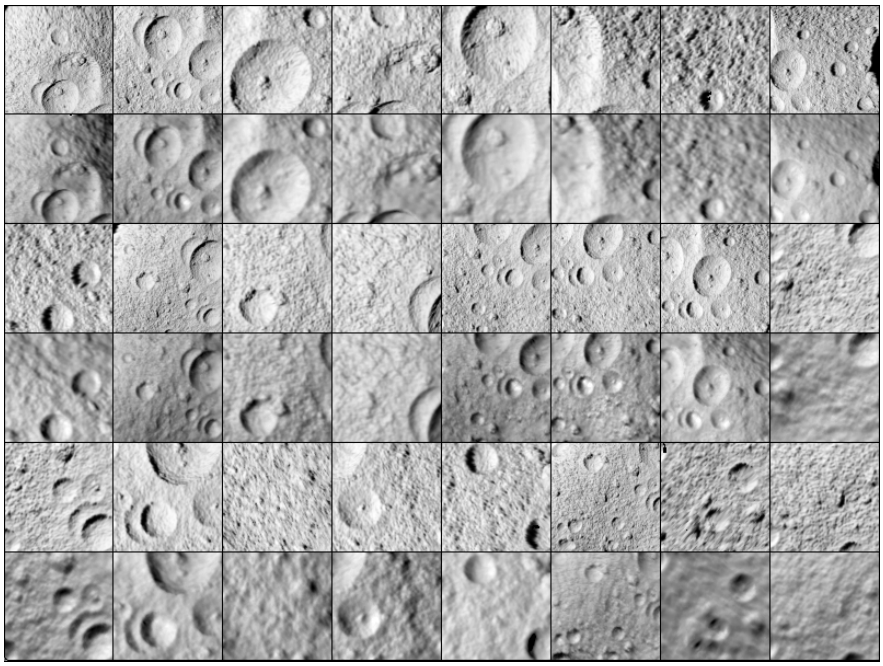

Figure 17. Auto-registration display for a wide-angle image

For the seven images, the rms spacecraft location residual was 2.9 m in the line-of-sight direction and 0.76 m in the cross line-of sight direction. The pointing errors were still dominated by the a priori. By waiting 15 minutes more to find the landmark maps on the limbs of the seven images, the rms line-of-sight error is reduced to 2.4 m.

The results above do not include image-to-image correlations in the form of expected inertial space differences in spacecraft location for neighboring pictures, the fourth term in equation 10). Ultimately, these differences will be determined by fitting the nominal spacecraft locations to the dynamical model, such as the gravitational field. In this case, a simple linear fit as a function of time was used, with the appropriate formal rate uncertainties, and a time cutoff of ±4000 seconds. Thus for each of the seven narrow angle sequences, an image was correlated with the two before and the two after. For both the 20 km and 7 km stations, the pointing errors were about 60 μrad in clock and cone, and 150 μrad in twist. The radial errors were 10.3 meters at 20 km and 4.1 meters at 7 km. The cross line-of-sight errors at the two distances were 1.16 meters and 0.66 meters respectively. These are actual errors, differences between the determined values and those used to construct the images. In all cases, they were within 30% of the formal uncertainties, which gives us confidence in the latter values. The formal uncertainty in landmark location was 21 cm per degree of freedom, while the rms post-fit residual was 27 cm.

An additional six wide-angle images were added, so that the time spacing of the approach sequence was 30 minutes, as in the narrow angle sequences. The image-to-image correlation brought the rms error down from 2.9 meters and 0.76 meters line of sight and cross line of sight respectively, to 1.66 m and 0.62 m without limbs and 1.46 m and 0.60 m with limbs. Notice that the solution can no longer be done individually for each image, since it is the sequence is processed as a whole.

The radial error was somewhat larger than expected from theoretical analysis of the uncertainties. It turned out that the origin of the “true” model was shifted by about a meter from the center of figure. When that correction was made, the errors dropped to 1.18 meters and 0.37 meters. Another possibility was that the ensemble of maps had not yet converged. Another iteration was performed to re-compute map locations and topography, using narrow angle data only. The wide-angle rms errors dropped to 0.84 meters along the line of sight and 0.30 meters across the line of sight. The narrow-angle errors were correspondingly reduced.

9. Lessons learned

Since this simulation was completed, much time has been spent going over ways to improve the procedures. For example, the camera pointing and spacecraft position in the pixel and line directions are degenerate when the spacecraft is far from the body, or close to it and nadir pointed. In fact, the determination of these components of spacecraft position is directly tied to the pointing as determined from the star tracker. For this reason, it is planned to place a very tight *a priori* on the cross line-of-sight spacecraft location at the 20 km and 7 km stations, and very loose ones on the corresponding camera

pointing. The Hayabusa project's range and twist uncertainties will be used, however, since the latter information is fundamental to estimating the pole.

Another post-simulation revelation came when the planetary constants file was being created for Itokawa. Inconsistencies in the results revealed that the wrong pole was used in the simulation. Since Ostro's pole was in the celestial coordinate frame, and the Spice procedures assume an Earth equatorial frame, the simulation's pole was off by 23 degrees. This in no way invalidates the results of the study, which verify that optical-only landmark navigation can provide sub-meter proximity positioning in real time.

The next step in the evolution of this technique will be to install the software that estimates position and orientation from a set of known L-maps onboard a spacecraft. The L-maps themselves will be estimated on the ground, and then uploaded to allow for autonomous approach and landing navigation. This capability is currently under development.

Acknowledgements

This work was carried out at the Jet Propulsion Laboratory, California Institute of Technology, under a contract with the National Aeronautics and Space Administration.

References

R.W. Gaskell (2001), "Automated Landmark Identification for Spacecraft Navigation," AAS paper 01-422, AAS/AIAA Astrodynamics Specialists Conf., Quebec.

R.W. Gaskell (2002), "Determination of Landmark Topography from Imaging Data," AAS paper 02-021, AAS/AIAA Astrodynamics Specialists Conf., Breckenridge.

R.W. Gaskell (2003), "Optical Only Determination of Small Body Shape and Topography," ISPRS WG IV/9, Houston.

R.W. Gaskell (2004), "High Resolution Shape and Topography of Eros - Preliminary Results From NEAR Imaging Data," AGU Spring Meeting, Montreal

R.W. Gaskell (2005), "Small Body Simulations for Navigation Approach and Landing," AIAA-2005-6813, SPACE 2005, Long Beach, CA

B. Hapke (1981), "Bidirectional Reflectance Spectroscopy, I. Theory," Journal of Geophysical Research 86, 3039-3054.

S.J. Ostro. et al. (2004), "Radar Observations of Asteroid 25143 Itokawa (1998SF36)," Meteoritics and Planetary Science, in press.

. S. Squyres and J. Veverka (1982), "Variation of Albedo with Solar-Incidence Angle on Planetary Surfaces," Icarus 50, 115-122.